Electronic chirality in the metallic ferromagnet $Fe_{1/3}TaS_2$

S. Fan,[1] I. Manuel,[2] Amal al-Wahish,[3] K. R. O'Neal,[3] K. A. Smith,[3] C. J. Won,[4] J. W. Kim,[5] S.-W. Cheong,[4,5] J. T. Haraldsen,[2] and J. L. Musfeldt[1,3]

[1]*Department of Physics and Astronomy, University of Tennessee, Knoxville, Tennessee 37996, USA*

[2]*Department of Physics, University of North Florida, Jacksonville, Florida 32224, USA*

[3]*Department of Chemistry, University of Tennessee, Knoxville, Tennessee 37996, USA*

[4]*Laboratory for Pohang Emergent Materials and Max Plank POSTECH Center for Complex Phase Materials, Pohang University of Science and Technology, Pohang 790-784, Korea*

[5]*Rutgers Center for Emergent Materials and Department of Physics and Astronomy, Rutgers University, Piscataway, New Jersey 08854, USA*

(Received 19 July 2017; revised manuscript received 25 September 2017; published 13 November 2017)

We bring together optical spectroscopy and first-principles calculations to reveal the electronic properties of the chiral ferromagnet $Fe_{1/3}TaS_2$. Signatures of chirality are superimposed upon a complex free-carrier response that emanates from both Ta and Fe bands. These include a honeycomb charge density pattern in the Fe layer and a hole → electron pocket crossover at the K point, low-energy excitations between spin split bands that cross the Fermi surface, and clustered rather than well-separated on-site and charge-transfer excitations. These findings advance the understanding of intercalation and symmetry breaking on the fundamental excitations in metallic chalcogenides.

DOI: 10.1103/PhysRevB.96.205119

I. INTRODUCTION

Research on engineered superlattice materials has blossomed in recent years due to the discovery of unexpected properties deriving from interface effects [1–4]. Naturally occurring superlattices like intercalated oxides and chalcogenides are of contemporary interest as well. Examples include the chiral helimagnets $Cr_{1/3}NbS_2$ and $[Pb_2BiS_3][AuTe_2]$, superconducting Pd-intercalated $IrTe_2$, and interlayer I-doped $BiOIO_3$ nanoplates [5–9]. The chiral ferromagnet $Fe_{1/3}TaS_2$ attracted our attention in this context [10]. This system is based upon 2H-TaS_2 [11,12] and has a set of stable, well-ordered intercalation plateaus at $x = 1/4$ and $1/3$ [Figs. 1(a)–1(c)] [10]. The pattern of Fe centers is responsible for the noncentrosymmetric, chiral space group of the $x = 1/3$ system [10]. Intercalation suppresses the charge-density wave transitions [13], and magnetic transitions arise at 160 and 35 K for the $x = 1/4$ and $1/3$ materials, respectively [10,14,15]. Large magnetoresistances and high coercivities have been reported as well [16]. Moreover, the atomically thin Fe layers in Fe_xTaS_2 display fascinating domain wall symmetries and domain patterns [10]; that, in the $x = 1/3$ system is $Z_2 \times Z_3$ [17]. In this paper, we show that signatures of chirality in $Fe_{1/3}TaS_2$ are deeply and subtly embedded within the electronic structure, reminiscent of the hidden Fermi surface nesting that causes charge-density wave ordering in low-dimensional materials [18].

To explore intercalation effects on the fundamental excitations of a chiral ferromagnet, we measured the spectroscopic response of $Fe_{1/3}TaS_2$ and compared our findings with the $x = 0$ and $1/4$ compounds and complementary first-principles calculations. The main finding is that there is a strong influence of the Fe layer on the properties of the compound, perhaps stronger than what would be expected for van der Waals interlayer bonding. Strikingly, separation of chalcogenide slabs by atomically thin layers of iron introduces a second free-carrier response due to a peak in the density of states at the Fermi level along with a set of localized bands that are connected to the density and pattern of the Fe centers. Symmetry breaking in $Fe_{1/3}TaS_2$ is evident in charge-density patterns that progress from triangular to Kagome to honeycomb, the hole → electron pocket crossover near the K point, and the characteristic set of low-energy electronic excitations between spin split bands that cross the Fermi surface. Signatures of chirality are firmly embedded in the bound carrier excitations as well, which we analyze by tracking trends in the hybridized Fe- and Ta-containing bands. Importantly, these effects are exposed in a metallic system, so in addition to providing opportunities to compare correlation vs spin-orbit effects in Fe-containing chalcogenides [19–21], they reveal ideas that may be useful in the hunt for metallic ferroelectrics [22,23].

II. METHODS

Single crystals of Fe_xTaS_2 ($x = 1/4$ and $1/3$) were grown by chemical vapor transport techniques as described previously, and the Fe concentration was confirmed by magnetization [10]. We measured ab-plane reflectance using a series of spectrometers (4 meV–6.5 eV; 4.2–300 K) and employed a Kramers-Kronig analysis to extract the optical constants. Traditional peak-fitting techniques were also employed as appropriate. Computational work was performed using density functional theory provided by Atomistix ToolKit [24,25]. Using a spin-polarized generalized gradient approach with an on-site potential (SGGA+U), the electronic structure, density of states (DOS), and electron density were determined [26]. The onsite potential localizes the Fe electrons that contribute to the overall magnetic moment; we find 3.8 μ_B.

III. RESULT AND DISCUSSION

Figures 2(a) and 2(b) display the reflectance and optical conductivity of $Fe_{1/4}TaS_2$ and $Fe_{1/3}TaS_2$ compared with that of 2H-TaS_2 [11]. Intercalation dramatically changes the character of the optical conductivity. The trend is nonmonotonic, with the Drude response in the $x = 1/3$ system being more robust

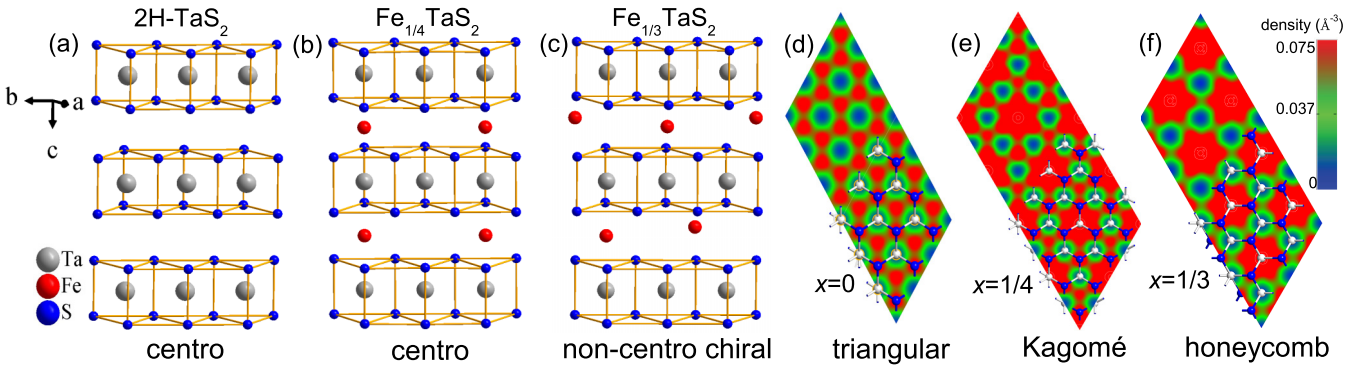

FIG. 1. (a) Crystal structure of 2H-TaS_2 in the centrosymmetric $P6_3/mmc$ space group [27]. Ta^{4+} is at the center of a prism formed by six S^{2-} centers. (b) $Fe_{1/4}TaS_2$ also belongs to the $P6_3/mmc$ space group [10]. Each Fe center is octahedrally coordinated by six S^{2-} atoms. Stacking along c is AA type, yielding an expanded $2a \times 2a$ superlattice. (c) The structure of $Fe_{1/3}TaS_2$ is noncentrosymmetric and chiral (space group $P6_322$) [10]. Stacking along c is alternating (AB) type, yielding a $\sqrt{3}a \times \sqrt{3}a$ superlattice. (d)–(f) Projected charge density in the Fe plane for 2H-TaS_2, $Fe_{1/4}TaS_2$, and $Fe_{1/3}TaS_2$.

than for $x = 1/4$. Although this family of transition metal dichalcogenides is metallic, there are several small structures between 10 and 40 meV in the $x = 1/3$ compound that are not completely screened. They are present at 300 K but much more evident at low temperature [Figs. 2(c) and 2(d)]. The energy scale of these features is consistent with assignment as either phonons or electronic excitations between spin split bands. Temperature effects are overall modest.

Figure 2(e) displays a close-up view of the Drude-Lorenz fit to the optical conductivity of $Fe_{1/3}TaS_2$. Two Drude functions are needed to capture the response. The two-component nature of the free carrier behavior is due to the superposition of Fe and TaS_2 layer conductivities. The former has only about 1% of the oscillator strength of the latter. Compared to 2H-TaS_2, intercalation at the $x = 1/3$ level reduces the oscillator strength associated with the TaS_2 slab by approximately 40%, the plasma frequency by 15%, and the relaxation time by 35% (Table I). These trends quantify the fact that the TaS_2 layers are well isolated between Fe sheets. The Drude associated with the Fe layer is much narrower than that deriving from the Ta bands (which so prominently cross the Fermi surface).

A similar situation arises in $Fe_{1/4}TaS_2$, where fits to the optical response require two Drude oscillators. The metallic character is weaker than in the $x = 1/3$ system due to a different degree of mixing of the hybridized Ta + Fe d bands crossing the Fermi level. The Fe Drude is extremely narrow because the distance between Fe centers is quite large (6.614 Å for $x = 1/4$ vs 5.737 Å for $x = 1/3$), an effect that is evident in the charge density patterns. The lower density of atomic centers in the Fe sheet of the $x = 1/4$ material reduces overlap and increases the relaxation time (Table I). An oscillator strength analysis [Fig. 2(f)] provides additional evidence for a narrow Drude [31].

Turning our attention to the higher energy portion of the spectra, the pattern of well-separated on-site and charge-transfer excitations in the $x = 1/4$ material and the superimposed set of features in the $x = 1/3$ system seem dramatically different [Fig. 2(h)]. Closer examination, however, reveals that the localized and charge transfer excitations reflect the trend in the Fe levels. In the $x = 1/4$ system, we assign the band centered at 0.7 eV as a minority channel Ta $d \rightarrow$ Ta d excitation and those at 2.0 and 2.6 eV as Ta $d \rightarrow$ Fe d charge transfer excitations in the spin-down channel. The 3.2 eV peak is assigned to minority channel Fe $d \rightarrow$ Fe d excitations. Four excitations also appear in the spectrum of the $x = 1/3$ material, but they are clustered together at 1.2, 1.6, 2.2, and 3 eV [Fig. 2(g)], and the assignment changes somewhat. These excitations are superimposed at overall higher energy because the Fe bands have moved up in energy and are significantly more disperse compared to those in the $x = 1/4$ system. This allows the Fe levels to hybridize with the Ta bands around 2 eV. There is also a band centered near 5.3 eV in both materials. In 2H-TaS_2, it is assigned as a Ta $5d_{z^2}$ conduction band to S $3p$ valence band excitation [32]. The characterization shifts to greater d-band contributions in the $x = 1/4$ and 1/3 systems.

Figure 3 displays the calculated electronic band structure and projected density of states for the three systems of interest. We used this band structure to assign all of the optical excitations in these materials. Where comparable, our findings are in good agreement with prior work [13,33,34]. In our analysis of 2H-TaS_2, there exist two distinct Ta-derived bands crossing the Fermi level [Fig. 3(a)] that are characteristic of Dirac lines [35]. These bands make the system metallic and produce excitations to the bands near 3.5 eV. These aspects of the electronic structure remain recognizable even with

TABLE I. Drude parameters of Fe_xTaS_2 ($x = 0$, 1/4, 1/3) obtained from fits to the optical conductivity at 300 K. Error bars on the fit parameters are on the order of 1%, with the exception of the very narrow Fe Drude in the $x = 1/4$ material, where the error bars are on the order of 5%.

Materials	Oscillator strength (eV^2)	Plasma freq (eV)	Relaxation time (s)
2H-TaS_2	0.18	1.19	2.5×10^{-14}
$Fe_{1/4}TaS_2$			
Fe Drude	0.37×10^{-3}	0.02	3.5×10^{-12}
TaS_2 Drude	0.038	0.66	1.3×10^{-14}
$Fe_{1/3}TaS_2$			
Fe Drude	1.78×10^{-3}	0.24	7.5×10^{-13}
TaS_2 Drude	0.11	1.02	1.6×10^{-14}

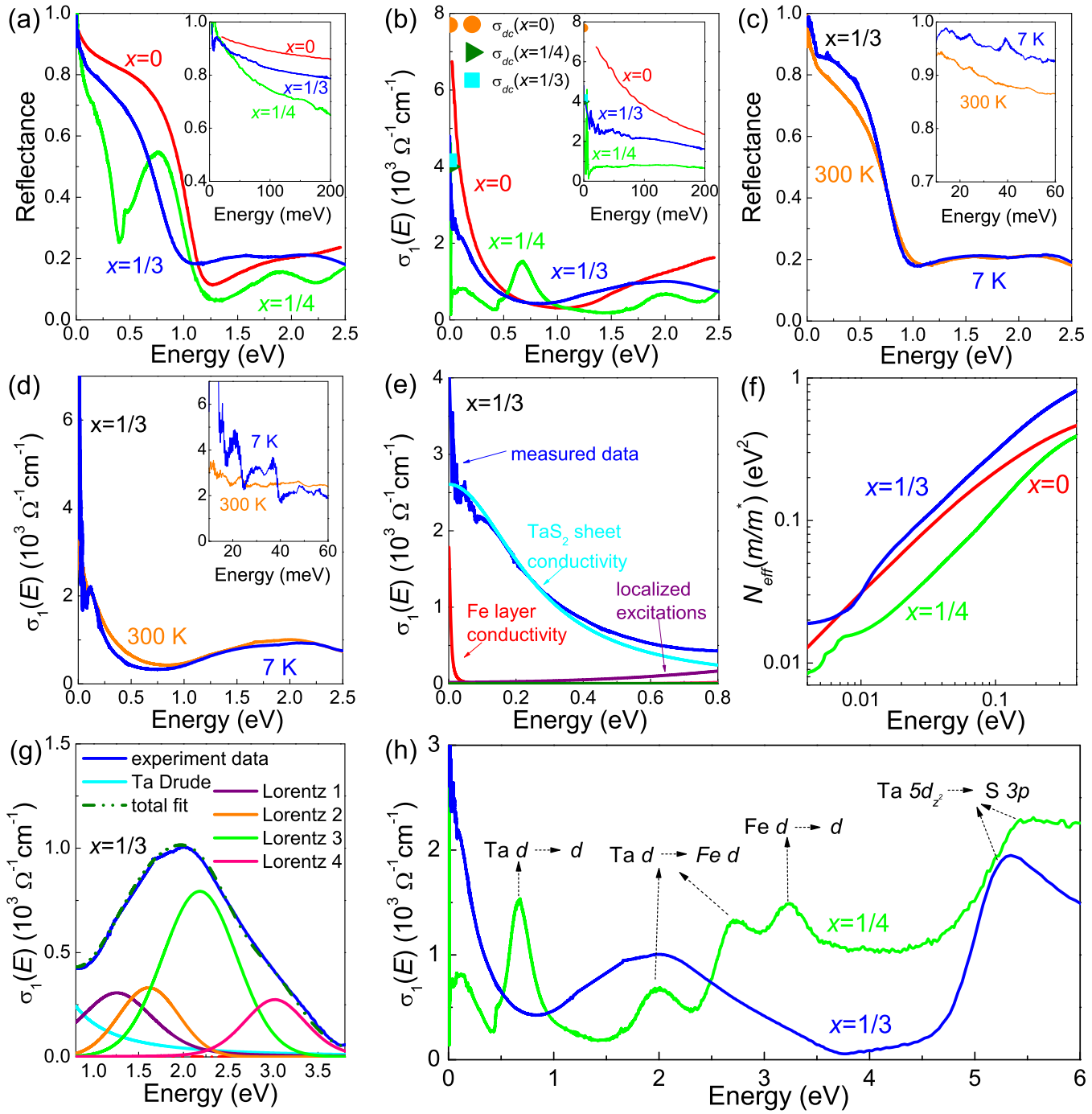

FIG. 2. (a) Reflectance of $Fe_{1/4}TaS_2$, $Fe_{1/3}TaS_2$, and 2H-TaS_2. The 2H-TaS_2 data is reproduced from Ref. [11]. Inset: close-up view of the low energy response. (b) Optical conductivity of these materials. Literature values of the *dc* conductivity [28–30] are also plotted; $\sigma_1(E)$ extrapolates to these values reasonably well. (c) Reflectance of $Fe_{1/3}TaS_2$ at 300 and 7 K. (d) Optical conductivity of the $x = 1/3$ material at 300 and 7 K. Inset displays a close-up view of low energy response. (e) Close-up view of the two Drude oscillators needed to fit the response of $Fe_{1/3}TaS_2$. (f) Oscillator strength sum rule for the $x = 0$, 1/4, and 1/3 compounds. (g) Drude-Lorentz fit of the localized excitations in $Fe_{1/3}TaS_2$. (h) Optical conductivity of $Fe_{1/4}TaS_2$ and $Fe_{1/3}TaS_2$ highlighting the difference in the localized excitations.

the addition of Fe and hybridization with Fe-related bands. Electron and hole pockets are predicted at the M and K points, respectively.

Introduction of an atomically thin layer of Fe into the van der Waals gap modifies the electronic structure profoundly. Our calculations employ a Hubbard U (similar to Ref. [13]), which acts to localize the Fe bands, leaving only a remnant of Fe density at the Fermi level. Localization is thus responsible for the weak metallicity of the Fe layer in the $x = 1/4$ system [evidenced by a small but distinct second Drude oscillator in the inset of Fig. 2(b)]. When Fe density increases ($x = 1/3$), orbital overlap is improved, and the localized Fe bands are swept upward. This gives greater metallicity to the Fe layer because density at the Fermi surface is larger and, at the same

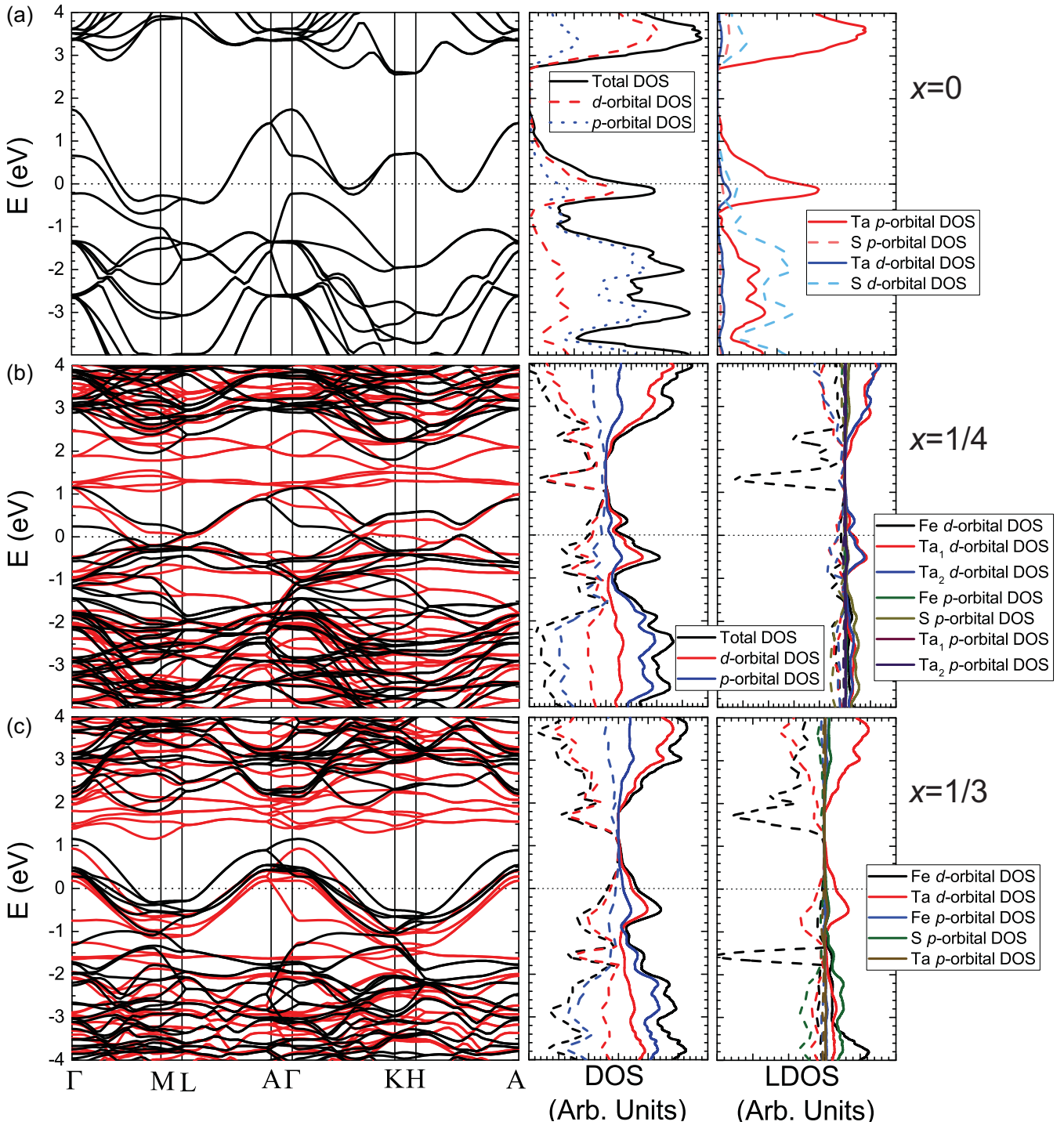

FIG. 3. Calculated electronic band structure and DOS (total, partial, and local) for (a) 2H-TaS_2, (b) $Fe_{1/4}TaS_2$, and (c) $Fe_{1/3}TaS_2$. The black and red bands in the electronic structure and the solid and dashed lines in the DOS plots denote the spin-up and spin-down channels, respectively.

time, raises the energy of the localized Fe bands, which allows them to hybridize with the Ta-derived bands. This process strengthens the Fe-derived Drude and makes the localized excitations seem to disappear. The persistence of the Dirac lines produced by the TaS_2 slabs at high-symmetry points demonstrates that these modifications are due to differences in overall electronic behavior rather than intercalation-induced structural changes.

To further examine the connection between symmetry and electronic structure, we projected the charge density onto the plane defined by the Fe centers [Figs. 1(d)–1(f)]. With these renderings, we see that, as the Fe concentration increases, the overlap between Fe sites becomes stronger and more direct, and at the 1/3 level, the Fe centers even move out of the way of the S ions allowing for more direct orbital overlap. Thus, while the dominant Drude response is connected

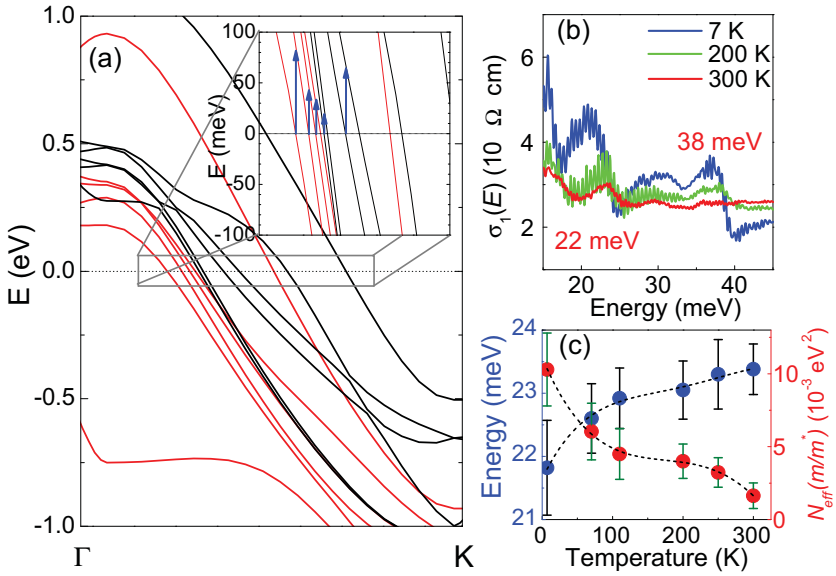

FIG. 4. (a) Close-up view of the band structure of $Fe_{1/3}TaS_2$ between the Γ and K points. Inset: low-energy excitations on the order of a few tens of meV due to the band splitting. (b) Temperature dependence of the optical conductivity of the $x = 1/3$ materials in the vicinity of the 22 and 38 meV excitations. (c) Peak position and oscillator strength of the 22 meV feature as a function of temperature.

with free carriers in the Ta bands, the Fe ions introduce a second metallic signature—consistent with our spectroscopic findings. Remarkably, these contour plots also reveal a progression from a triangular ($x = 0$) to Kagome ($x = 1/4$) to honeycomb ($x = 1/3$) charge density pattern [Figs. 1(d)–1(f)]. The latter is (ironically) indicative of increased symmetry in the Fe plane, even though the overall crystal symmetry is reduced.

Another consequence of the evolving charge density pattern can be seen by comparing the electronic structure at the M and K symmetry points. In the centrosymmetric case [Figs. 3(a) and 3(b)], the M point sports an electron pocket whereas the K point has a hole pocket. However, in the noncentrosymmetric case [Fig. 3(c)], both locations host electron pockets. This hole to electron pocket crossover at the K point, while certainly not simple, may be observable in a Hall measurement and could have important implications for the field of valleytronics [36]. We note that the crossover to electron pockets in $Fe_{1/3}TaS_2$ is not just due to increased carrier density from the Fe centers (although additional density does accumulate at the K point) but rather due to the manner in which Fe breaks crystal symmetry. Therefore, a gating experiment that merely raises and lowers the Fermi energy against a rigid band structure would not show this effect.

Finally, we point out that broken inversion symmetry in the $x = 1/3$ material is predicted to lift the spin degeneracy of the electronic bands near the Fermi surface [Fig. 4(a)]. The energy scale of this splitting is on the order of tens of meV, consistent with the aforementioned features at 22 and 38 meV in the optical conductivity. Figure 4(b) displays a close-up view of these structures. Although the excitation energies are in line with what might be expected for electronic band splitting, assignment is not straightforward because they are also consistent with phonon positions [37]. As shown in Figs. 4(b) and 4(c), decreasing temperature red shifts the 22 and 38 meV structures and increases the oscillator strength [38]. Both trends differ from what is expected for phonons on a conducting background [39]. Moreover, we do not anticipate significant differences in phonon effects between the $x = 1/4$ and 1/3 materials, which again argues against a phonon interpretation. Returning to our picture of low-energy spin split electronic excitations, there are several bands crossing the Fermi energy with vertical band-to-band transitions in the correct energy range [Fig. 4(a)]. Recent models of Rashba splitting in BiTeI [40] suggest that thermal expansion and electron-phonon coupling effects combine to reduce the effective Rashba parameter and smear the gap(s) at elevated temperatures. Of course, while the 2H structures technically lack inversion symmetry, they do have a vertical mirror plane, so we do not anticipate the same kind of strong inversion-breaking Rashba effects that are observed in BiTeI [41]. Additional evidence that the 22 and 38 meV excitations may be electronic in origin comes from the $x = 1/4$ system where these features are not observed.

IV. CONCLUSION

To summarize, we combined optical spectroscopy and first-principles calculations to reveal intercalation and symmetry breaking effects in the noncentrosymmetric, chiral ferromagnet $Fe_{1/3}TaS_2$. The main finding is that there is a strong influence of the Fe layer on the properties of the compound, perhaps stronger than what would be expected for van der Waals interlayer bonding. Signatures of chirality include a honeycomb charge density pattern and hole → electron pocket crossover, low-energy excitations between spin split bands, and overlapping onsite and charge transfer excitations. These findings are useful for the development of low symmetry multifunctional chalcogenides.

ACKNOWLEDGMENTS

Research at Tennessee is supported by the US Department of Energy, Office of Basic Energy Sciences, Materials Science Division under Award No. DE-FG02-01ER45885. J.T.H. acknowledges funding from the Institute for Materials Science at Los Alamos National Laboratory. Work at Rutgers is supported by the NSF-DMREF Program (DMR-1629059). Research at Postech is funded by the Max Planck POSTECH/KOREA Research Initiative Program No. 2011-0031558 through NRF of Korea funded by MEST. We thank A. V. Balatsky and D. H. Vanderbilt for useful discussions.

[1] H. Y. Hwang, Y. Iwasa, M. Kawasaki, B. Keimer, N. Nagaosa, and Y. Tokura, Nat. Mater. **11**, 103 (2012).

[2] S. Singh, J. T. Haraldsen, J. Xiong, E. M. Choi, P. Lu, D. Yi, X.-D. Wen, J. Liu, H. Wang, Z. Bi, P. Yu, M. R. Fitzsimmons, J. L. MacManus-Driscoll, R. Ramesh, A. V. Balatsky, J.-X. Zhu, and Q. X. Jia, Phys. Rev. Lett. **113**, 047204 (2014).

[3] J. A. Mundy, C. M. Brooks, M. E. Holtz, J. A. Moyer, H. Das, A. F. Rebola, J. T. Heron, J. D. Clarksen, S. M. Disseler, Z. Liu, A. Farhan, R. Held, R. Hovden, E. Padgett, Q. Mao, H. Paik, R. Misra, L. F. Kourkoutis, E. Arenholz, A. Scholl, J. A. Borchers, W. D. Ratcliff, R. Ramesh, C. J. Fennie, P. Schiffer, D. A. Muller, and D. G. Schlom, Nature **537**, 523 (2016).

[4] B.-W. Li, M. Osada, Y. Ebina, S. Ueda, and T. Sasaki, J. Am. Chem. Soc. **138**, 7621 (2016).

[5] Y. Sun, T. Xiong, F. Dong, H. Huang, and W. Cen, Chem. Commun. **52**, 8243 (2016).

[6] Y. Togawa, T. Koyama, K. Takayanagi, S. Mori, Y. Kousaka, J. Akimitsu, S. Nishihara, K. Inoue, A. S. Ovchinnikov, and J. Kishine, Phys. Rev. Lett. **108**, 107202 (2012).

[7] N. J. Ghimire, M. A. McGuire, D. S. Parker, B. Sipos, S. Tang, J.-Q. Yan, B. C. Sales, and D. Mandrus, Phys. Rev. B **87**, 104403 (2013).

[8] J. J. Yang, Y. J. Choi, Y. S. Oh, A. Hogan, Y. Horibe, K. Kim, B. I. Min, and S.-W. Cheong, Phys. Rev. Lett. **108**, 116402 (2012).

[9] L. Fang, J. Im, W. DeGottardi, Y. Jia, A. Glatz, K. A. Matveev, W.-K. Kwok, G. W. Crabtree, and M. G. Kanatzidis, Sci. Rep. **6**, 35313 (2016).

[10] Y. Horibe, J. Yang, Y. H. Cho, X. Luo, S. B. Kim, Y. S. Oh, F. T. Huang, T. Asada, M. Tanimura, D. Jeong, and S. W. Cheong, J. Am. Chem. Soc. **136**, 8368 (2014).

[11] W. Z. Hu, G. Li, J. Yan, H. H. Wen, G. Wu, X. H. Chen, and N. L. Wang, Phys. Rev. B **76**, 045103 (2007).

[12] S. S. P. Parkin and R. H. Friend, Philos. Mag. B **41**, 65 (1980).

[13] S. Mankovsky, K. Chadova, D. Kodderitzsch, J. Minar, H. Ebert, and W. Bensch, Phys. Rev. B **92**, 144413 (2015).

[14] T. Danz, Q. Liu, X. D. Zhu, L. H. Wang, S. W. Cheong, I. Radu, C. Ropers, and R. I. Tobey, J. Phys.: Condens. Matter **28**, 356002 (2016).

[15] Q. Liu, X. D. Zhu, L. H. Wang, S. W. Cheong, and R. I. Tobey, J. Phys.: Condens. Matter **28**, 194002 (2016).

[16] W. J. Hardy, C.-W. Chen, A. Marcinkova, H. Ji, J. Sinova, D. Natelson, and E. Morosan, Phys. Rev. B **91**, 054426 (2015).

[17] F. T. Huang and S. W. Cheong, Nat. Rev. Mater. **2**, 17004 (2017).

[18] M.-H. Whangbo, E. Canadell, P. Foury, and J. P. Pouget, Science **252**, 96 (1991).

[19] C. C. Homes, A. Akrap, J. S. Wen, Z. J. Xu, Z. W. Lin, Q. Li, and G. D. Gu, Phys. Rev. B **81**, 180508(R) (2010).

[20] Q. M. Si, R. Yu, and E. Abrahams, Nat. Rev. Mater. **1**, 16017 (2016).

[21] D. S. Inosov, C. R. Phys. **17**, 60 (2016).

[22] A. Filippetti, V. Fiorentini, F. Ricci, P. Delugas, and J. Iniguez, Nat. Comm. **7**, 11211 (2016).

[23] Y. G. Shi, Y. F. Guo, X. Wang, A. J. Princep, D. Khalyavin, P. Manuel, Y. Michiue, A. Sato, K. Tsuda, S. Yu, M. Arai, Y. Shirako, M. Akaogi, N. Wang, K. Yamaura, and A. T. Boothroyd, Nat. Mater. **12**, 1024 (2013).

[24] Atomistix ToolKit version 13.8, QuantumWise A/S, www.quantumwise.com.

[25] J. M. Soler, E. Artacho, J. D. Gale, A. Garcia, J. Junquera, P. Ordejon, and D. Sanchez-Portal, J. Phys.: Condens. Matter **14**, 2745 (2002).

[26] Energy minimization tolerance of $< 10^{-5}$ Hartree with a k-point sampling of 10 x 10 x 10 were used along with potentials of $U_{Ta} = 2.5$ eV and $U_{Fe} = 4.0$ eV.

[27] A. Meetsma, G. A. Wiegers, R. J. Haange, and J. L. de Boer, Acta Crystallogr. Sect. C **46**, 1598 (1990).

[28] S. S. P. Parkin and R. H. Friend, Phys. B (Amsterdam) **99**, 219 (1980).

[29] J. G. Checkelsky, M. Lee, E. Morosan, R. J. Cava, and N. P. Ong, Phys. Rev. B **77**, 014433 (2008).

[30] M. Naito and S. Tanaka, J. Phys. Soc. Jpn. **51**, 219 (1982).

[31] A phonon is also present in the vicinity.

[32] S. S. P. Parkin and S. C. Bayliss, J. Phys. C **15**, 6851 (1982).

[33] J. Dijkstra, P. J. Zijlema, C. F. van Bruggen, C. Haas, and R. A. de Groot, J. Phys.: Condens. Matter **1**, 6363 (1989).

[34] L. F. Mattheiss, Phys. Rev. B **8**, 3719 (1973).

[35] R. M. Geilhufe, A. Bouhon, S. S. Borysov, and A. V. Balatsky, Phys. Rev. B **95**, 041103 (2017).

[36] J. R. Schaibley, H. Yu, G. Clark, P. Rivera, J. S. Ross, K. L. Seyler, W. Yao, and X. Xu, Nat. Rev. Mater. **1**, 16055 (2016).

[37] W. G. McMullan and J. C. Irwin, Can. J. Phys. **62**, 789 (1984).

[38] These trends are also apparent in the raw reflectance spectra [inset, Fig. 2(c)].

[39] J. Choi, J. L. Musfeldt, J. He, R. Jin, J. R. Thompson, D. Mandrus, X. N. Lin, V. A. Bondarenko, and J. W. Brill, Phys. Rev. B **69**, 085120 (2004).

[40] B. Monseratt and D. H. Vanderbilt, Phys. Rev. Mater. **1**, 054201 (2017).

[41] C. Martin, E. D. Mun, H. Berger, V. S. Zapf, and D. B. Tanner, Phys. Rev. B **87**, 041104 (2013).